Input-Output Analysis of a Separated Flow Past a Flat Plate

Hao Zhang*, Clarence Rowley†
Mechanical and Aerospace Engineering, Princeton University , Princeton, NJ, 08544

Wen Wu‡, Charles Meneveau§, and Rajat Mittal¶
Mechanical Engineering, Johns Hopkins University, Baltimore, MD, 21218

The response of a separated flow to external forcing is investigated using input-output analysis. A laminar separation bubble is induced on the flow past a flat plate by imposing an adverse pressure gradient. We study the response of spanwise-constant perturbations to both global body forcing and local body forcing. Input-output analysis (also referred to as resolvent analysis) uses a linear operator that maps the external forcing to the response of the flow field. For this flow forced at a single frequency, the linear operator is closely approximated by an operator of rank one, and describes the optimal spatial forcing for which the resulting response has maximum amplification. Input-output analysis gives useful information about optimal actuator placement and optimal actuation frequency. It is found that the flow response is maximized when forcing at the natural frequency of the separation bubble. The optimal response mode implies that the separation bubble is receptive to upstream body forcing. The optimal forcing mode indicates that body forcing should be applied upstream of the separation bubble, and gives information about the size and shape of the region where forcing should be applied, in order to maximize the response in the separation bubble.

I. Introduction

Flow separation is usually an undesirable phenomenon in aerodynamic applications because it reduces lift and increases (pressure) drag [1]. The complicated nonlinear dynamics of flow separation are characterized by Kelvin-Helmholtz instability, wake shedding, and separation bubble oscillations [1]. Efforts have been devoted to design control methods to suppress separation and reattach a separated flow. A number of studies try to find the optimal actuation parameters by searching the parameter space: see [2–5] for example. Parameter-searching control methods usually require huge experimental or simulation efforts, and provide only limited physical insights about the problem. Among various separation control methods, zero-net-mass-flux (ZNMF) actuators are simple to implement and have been shown to be effective in reducing flow separation [3, 6–9].

Input-output analysis was introduced to the fluid community to study the response of a flow field to disturbances [10, 11]. This approach uses the transfer function (a linear operator) from the input forcing (including nonlinear advective forcing, and any other external forcing) to the output response (velocity and pressure field). This linear operator is often low rank (sometimes approximately rank-one), and from it one can deduce the optimal forcing mode that actuates the optimal response that has maximum amplification, at any given forcing frequency. Input-output analysis, also referred to as resolvent analysis, has been used for a wide range of problems [12–15], ranging from pipe turbulent control to building reduced-order models. A review of various applications is presented in [16].

The focus of this paper is to better understand the physics of a separated flow, with the ultimate objective of controlling the flow. We consider a laminar boundary layer with a separation bubble along a flat plate. The separation is induced by a pressure gradient imposed through suction and blowing at the upper wall of the numerical domain. The forcing and response determined by input-output analysis can be very useful, since the optimal forcing and response can be used to guide placement of actuators and other aspects of the control design. Input-output analysis has been utilized for design of airfoil separation control [17], in which localized unsteady thermal actuation is applied near the leading edge. A previous study has looked into the response mode of incompressible jets to both body forcing and boundary forcing [13]. In the present work, we actuate the separated flow by both global and local body forcing.

*PhD Candidate and AIAA Member
†Professor and AIAA Associate Fellow
‡Postdoctoral Fellow and AIAA Member
§Professor and AIAA Member
¶Professor and AIAA Associate Fellow

II. Methodology

A. Flow setup and numerical simulation

In this paper we study a laminar boundary layer with a separation bubble induced by an adverse pressure gradient. The pressure gradient is imposed by suction and blowing on the top boundary, as shown in Fig. 1. This configuration has been widely studied as a proxy for separation in the flow past a wing at high angle of attack, because it isolates the effects of separation from other geometric effects such as wall curvature [18].

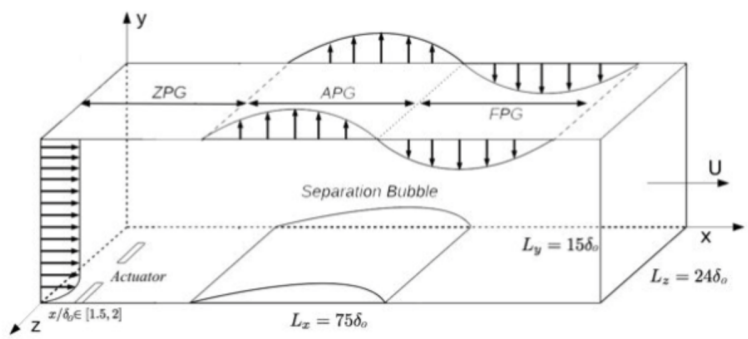

Fig. 1 Sketch of separated flow on a flat plate (not to scale). Adapted from [19].

The numerical simulation of the three-dimensional incompressible Navier-Stokes equations is performed with a second-order finite difference code ViCar3D [20]. Further details about the numerical schemes of the solver can be found in [19, 21]. The flow variables are nondimensionalized by the free-stream velocity $U_{\infty,0}$, and the boundary thickness δ_0 of the Blasius velocity profile at the inlet of the flow domain. The Reynolds number of the flow is $Re = U_{\infty,0}\delta_0/\nu = 1000$, where ν is the kinematic viscosity. The size of the computational domain is $75\delta_0$ in the streamwise direction, $15\delta_0$ in the wall-normal direction, and $24\delta_0$ in the spanwise direction.

Blasius velocity profiles are imposed at the inlet, and a Neumann boundary condition is used at the outlet (zero normal derivative). A no-slip boundary condition is imposed at the bottom wall, and a suction-blowing boundary condition (for wall-normal velocity) is imposed at the top boundary. At the top boundary, the streamwise velocity is implied by a zero-spanwise-vorticity condition. Periodic boundary conditions are assumed in the spanwise direction. The pressure satisfies a Neumann boundary condition at all boundaries (zero derivative normal to the boundary).

A simulation with no forcing is performed, and that is denoted as the base case ("case B"). For this case, the flow field averaged in time and in the spanwise direction is shown in Fig. 2, along with the spanwise-averaged fluctuations (deviations from the time-averaged flow). The time and spanwise averaged field will be used as base flow in the input-output analysis. The spanwise velocity is not reported here because it is small and close to zero. The flow is mainly two-dimensional, along with small spanwise fluctuations. Observe first that the imposed adverse pressure gradient successfully induces a separation bubble. The separation bubble spans from $x = 10\delta$ to $x = 55\delta$. The fluctuation field is nonzero mainly in and behind the trailing edge of the separation bubble region. The time- and spanwise-averaged flow field is taken as the base flow for the input-output analysis. We then study the response of the fluctuation field to external body forcing.

B. Input-output analysis formulation

To formulate the input-output analysis, we start from the incompressible Navier-Stokes equations

$$\partial_t \tilde{\boldsymbol{u}} = -\tilde{\boldsymbol{u}} \cdot \nabla \tilde{\boldsymbol{u}} - \nabla \tilde{p} + \frac{1}{Re}\nabla^2 \tilde{\boldsymbol{u}}, \tag{1a}$$

$$\nabla \cdot \tilde{\boldsymbol{u}} = \boldsymbol{0}. \tag{1b}$$

The full flow field $(\tilde{\boldsymbol{u}}, \tilde{p})$ is decomposed into a base flow $(\bar{\boldsymbol{u}}, \bar{p})$, which is usually taken to be the mean flow or a steady solution of the Navier-Stokes equations, and a fluctuation field $(\boldsymbol{u}, p)$, and we derive an equation for the fluctuations. Letting $\tilde{\boldsymbol{u}} = \bar{\boldsymbol{u}} + \boldsymbol{u}, \tilde{p} = \bar{p} + p$ and substituting into Eq. (1), we obtain

$$\partial_t \boldsymbol{u} = L\boldsymbol{u} - \nabla p + \boldsymbol{f}, \tag{2a}$$

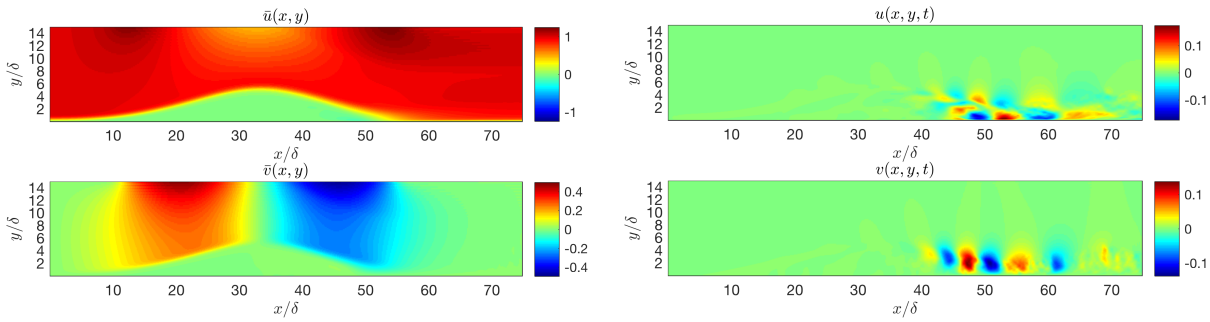

(a) **(b)**

Fig. 2 (a) Time and spanwise averaged field. (b) Spanwise averaged fluctuation field.

$$\nabla \cdot \boldsymbol{u} = \boldsymbol{0}, \tag{2b}$$

where

$$Lu = -\bar{\boldsymbol{u}} \cdot \nabla \boldsymbol{u} - \boldsymbol{u} \cdot \nabla \bar{\boldsymbol{u}} + \frac{1}{Re}\nabla^2 \boldsymbol{u},$$

and L is the linearized Navier-Stokes operator. The forcing term $\boldsymbol{f}$ includes all additional terms, including the nonlinear advective term and any external forcing terms such as body forcing and boundary forcing.

The governing equation of the fluctuation field is linear. Treating the nonlinear advective term and external forcing as input and velocity field as output, we can derive a state-space representation for the fluctuation field. If we define

$$q = \begin{bmatrix} \boldsymbol{u} \\ p \end{bmatrix}, \quad A = \begin{bmatrix} L & -\nabla \\ \nabla\cdot & 0 \end{bmatrix}, \quad M = \begin{bmatrix} 1 & 0 \\ 0 & 0 \end{bmatrix}, \quad B = \begin{bmatrix} 1 \\ 0 \end{bmatrix}, \quad C = \begin{bmatrix} 1 & 0 \end{bmatrix},$$

then Eq. (2) can be put into state-space form

$$M\partial_t q = Aq + B\boldsymbol{f}, \tag{3a}$$

$$\boldsymbol{u} = Cq, \tag{3b}$$

where $\boldsymbol{f}$ is the input and $\boldsymbol{u}$ is the output. If we consider sinusoidal forcing $\boldsymbol{f} = \hat{\boldsymbol{f}} e^{i\omega t}$, then both the state q and output $\boldsymbol{u}$ will be sinusoidal because the system is linear. Letting $\boldsymbol{u} = \hat{\boldsymbol{u}} e^{i\omega t}$ and substituting into Eq. (3), we obtain

$$\hat{\boldsymbol{u}} = H(i\omega)\hat{\boldsymbol{f}},$$

where

$$H(i\omega) = C(i\omega M - A)^{-1}B$$

is the transfer function from input ($\boldsymbol{f} = \hat{\boldsymbol{f}} e^{i\omega t}$) to output ($\boldsymbol{u} = \hat{\boldsymbol{u}} e^{i\omega t}$). The transfer function $H(i\omega)$ is the centerpiece of input-output analysis. (The operator $(i\omega M - A)^{-1}$ is called the resolvent operator, and analysis of this operator is often referred to as "resolvent analysis.") Notice that $H(i\omega)$ will be different for each different frequency ω. Keep in mind that $H(i\omega)$ is the transfer function from the forcing at a particular frequency ω to the response at the same frequency. In what follows, we fix a particular frequency ω, and we drop the explicit dependence of H on ω. However, note that the forcing and response modes we discuss below depend on the frequency ω.

Now let us consider the maximum amplification problem. We are interested in finding an input forcing with unit norm such that that the output has maximum norm:

$$\max_{\hat{\boldsymbol{f}}} \|\hat{\boldsymbol{u}}\|, \quad s.t. \quad \|\hat{\boldsymbol{f}}\| = 1,$$

where $\|\cdot\|$ denotes a suitable norm on the flow field $\hat{\boldsymbol{u}}$ and forcing term $\hat{\boldsymbol{f}}$. One can show (see, e.g., [22]) that the optimal forcing $\hat{\boldsymbol{f}}$ is an eigenvector of H^*H, where H^* denotes the adjoint of H: in particular, the optimal $\hat{\boldsymbol{f}}$ is the solution of

$$H^*H\hat{\boldsymbol{f}} = \sigma^2\hat{\boldsymbol{f}}$$

corresponding to the largest eigenvalue σ^2. The solution to the eigenvalue problem can be found from the singular value decomposition (SVD) of the linear operator

$$H = \sum_j \sigma_j \psi_j \phi_j^*,$$

where $\psi_i^* \psi_j = \delta_{ij}$, $\phi_i^* \phi_j = \delta_{ij}$, and $\sigma_j \geq 0$ is in descending order. The optimal forcing is the first right singular vector ϕ_1 and the optimal response is the first left singular vector ψ_1. The largest singular value σ_1 gives the corresponding amplification. For an arbitrary forcing $\hat{\boldsymbol{f}}$, the response $\hat{\boldsymbol{u}}$ can be written as

$$\hat{\boldsymbol{u}} = \sum_j \sigma_j \psi_j (\phi_j^* \hat{\boldsymbol{f}}),$$

where $\phi_j^* \hat{\boldsymbol{f}}$ is the projection of $\hat{\boldsymbol{f}}$ in the direction of ϕ_j. For many shear flows of practical interest [11–13, 22] the linear operator H can be closely approximated by an operator of rank one: $\sigma_1 \gg \sigma_{j\geq 2}$. A rank-one approximation of the response is then

$$\hat{\boldsymbol{u}} \approx \sigma_1 \psi_1 (\phi_1^* \hat{\boldsymbol{f}}), \tag{4}$$

and one expects this to be a close approximation of the response for a typical forcing $\hat{\boldsymbol{f}}$ (i.e., as long as the direction of forcing is not such that $\phi_1^* \hat{\boldsymbol{f}}$ is small).

The base flow is computed from the simulation previously described as "case B." We select a particular frequency ω, as the dominant frequency observed in the fluctuations for case B (as discussed in the next section). The transfer function $H(i\omega)$ is discretized with a finite-difference method, with appropriate boundary conditions for the fluctuations deduced from the simulation boundary conditions. After discretization, $H(i\omega)$ is a huge matrix of size 0.26 million by 0.26 million. For a matrix of this size, it is too cumbersome to compute the matrix inverse $(i\omega M - A)^{-1}$ explicitly, and accordingly, is extremely computational expensive to find the SVD of $H(i\omega)$ directly. Fortunately, we only need the first (few) singular values and singular vectors of H. The randomized SVD method of [23] is used to obtain the approximate leading singular values and singular vectors, without the need to explicitly compute the transfer function H or the resolvent $(i\omega M - A)^{-1}$.

C. Local body forcing

In the presentation above, the body force is global. However, it is usually not practical to impose a body force everywhere in space. We now consider external forcing as a local body force. The governing equation for the fluctuation field is

$$\partial_t \boldsymbol{u} = L\boldsymbol{u} - \nabla p + b(\boldsymbol{x})\boldsymbol{f}, \tag{5a}$$

$$\nabla \cdot \boldsymbol{u} = \boldsymbol{0}, \tag{5b}$$

with appropriate boundary conditions as specified in previous section. $b(\boldsymbol{x})$ embeds where the local body force is applied. In this study, we consider local body force in the upstream near the wall boundary (due to global forcing analysis). Following the derivation in section II.B, we can obtain a state-space representation similar to Eq. (3). For local forcing, we essentially have a different B matrix, which allows us to select which part of the flow field to apply forcing.

III. Results and Discussion

A. Modal decomposition analysis

We start with modal decomposition analysis of this problem. In particular, we consider three methods: discrete Fourier transform (DFT), proper orthogonal decomposition (POD) [24], and dynamic mode decomposition (DMD) [25]. They will provide insight about the coherent structures and main flow physics in the flow. Both three methods are based on temporal-spatial data (discrete velocity field measurements that evolve in time). DFT gives spatial mode associated with uniformly spaced frequencies ranging from zero to Nyquist frequency. POD extracts the most energetic spatial mode from data. DMD finds spatial mode that evolves in time with a fixed frequency and growth/decay rate. For more details and/or reviews about modal decomposition methods in fluid flows, see [16, 26].

First, we apply DFT to the fluctuation velocity field which consists of 300 snapshots with time step of $\triangle t = 2$. DFT frequencies, amplitudes and the first mode are shown in Fig. 3. It is revealed that there is a (non-dimensional) peak

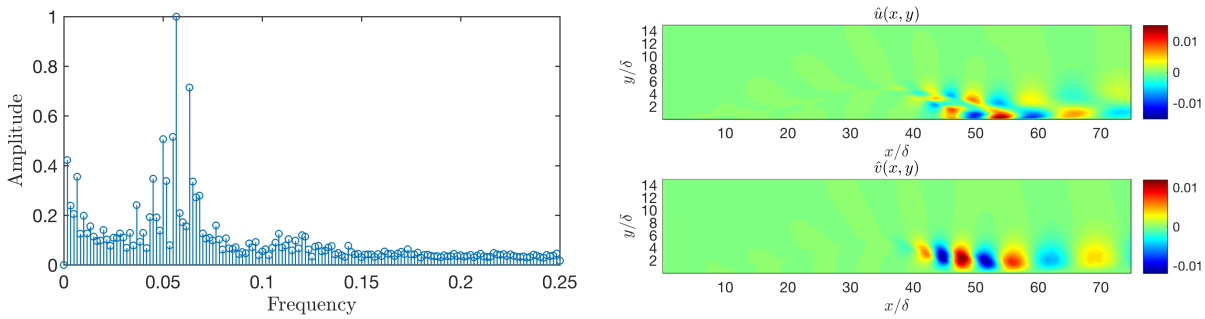

(a) **(b)**

Fig. 3 (a) DFT frequency and amplitude (normalized by maximum amplitude). (b) DFT mode $\hat{u}, \hat{v}$ (real part) associated with the peak frequency $f = 0.0567$.

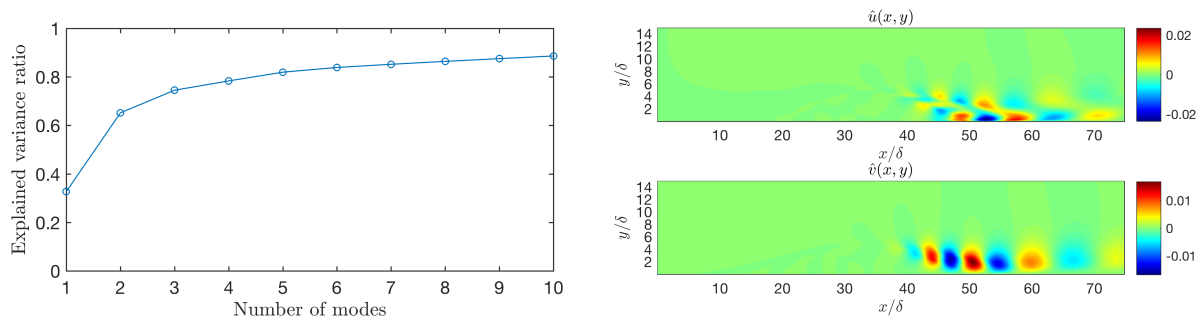

(a) **(b)**

Fig. 4 (a) Explained variance ratio with respect to number of POD modes. (b) First POD mode $\hat{u}, \hat{v}$.

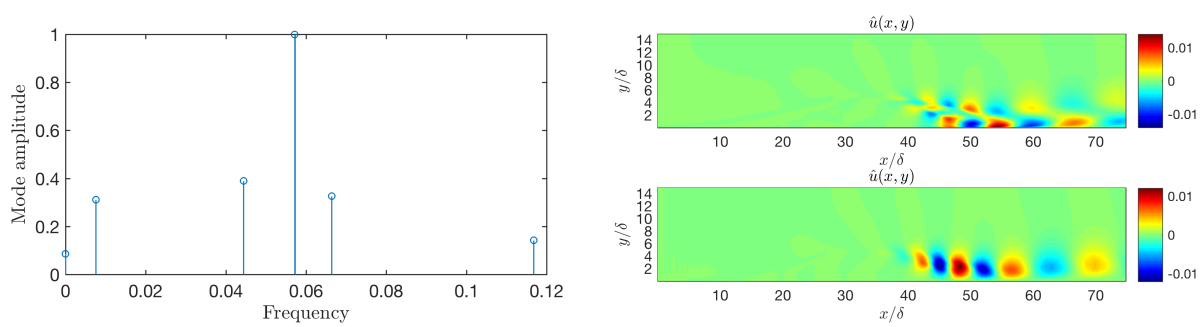

(a) **(b)**

Fig. 5 (a) DMD frequency and amplitude (normalized by maximum amplitude), largest amplitude occurs at $f = 0.0571$. (b) Dominant (largest amplitude) DMD mode $\hat{u}, \hat{v}$.

frequency at $f = 0.0567$. The associated mode resembles the fluctuation velocity field as shown in Fig. 2 (b). This Fourier mode indicates the coherent structure in this flow.

Next, we analyze the same fluctuation velocity field with POD. The result is presented in Fig. 4. We report the explained variance ratio, which is defined as

$$r_k = \sum_{j=1}^{k} \sigma_j^2 / (\sum_{j=1}^{N} \sigma_j^2), \tag{6}$$

where k is the number of modes used, N is the total number of modes, and σ_j is the j-th singular value (in descending order) of the snapshot matrix (whose column is the discrete velocity field). r_k quantifies how much energy are explained

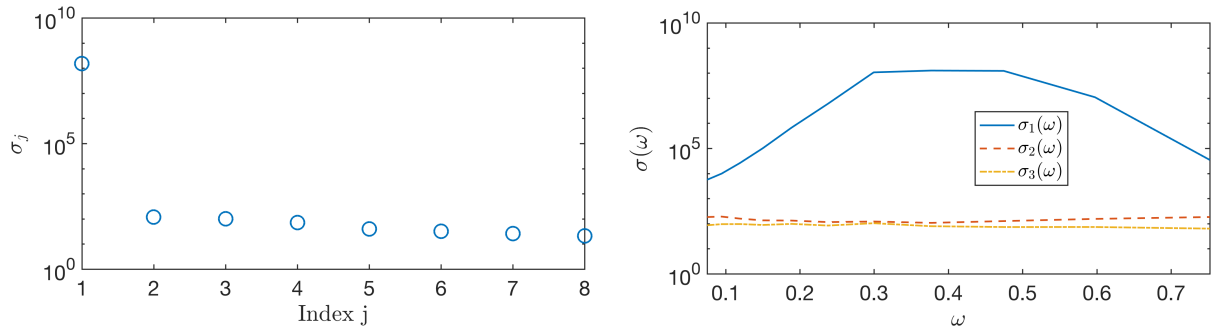

(a) **(b)**

Fig. 6 Global forcing result. (a) Singular values of the linear operator (transfer function) for $k_z = 0, \omega_p = 0.377$. (b) First three singular values of the transfer function for a range of frequency ω around ω_p. $k_z = 0$ is fixed.

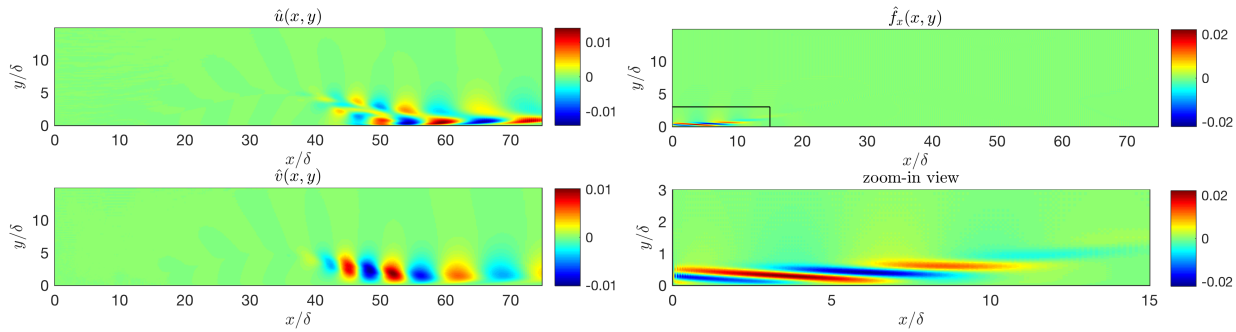

(a) **(b)**

Fig. 7 Global forcing result. (a) Streamwise and wall-normal optimal response mode $\hat{u}, \hat{v}$. $k_z = 0, \omega = 0.377$. (b) Streamwise optimal forcing mode $\hat{f}_x$ and zoom-in view in the region $(x/\delta, y/\delta) \in [0, 15] \times [0, 3]$.

by the first k POD modes. The first 10 POD modes explains about 90% of the total energy in the flow field. The first POD mode is shown in Fig. 4 (b), and this is considered as the dominate coherent structure in the fluctuation field. Observe that it is very similar to the dominant DFT mode.

Finally, DMD is used to find coherent structures in the fluctuation flow field. We first project the snapshots onto the subspace spaned by the leading POD modes of the snapshot matrix and then perform DMD in this subspace. This approach is more numerically stable and computationally efficient [26]. We use 11 POD modes, which amounts to keeping about 90% of the total energy in the snapshots. The result is shown in Fig. 5. DMD amplitude is defined as the magnitude of the coefficient when the initial condition is projected onto the DMD modes. DMD identifies a dominant frequency of $f = 0.0571$, which is (almost) the same as as DFT peak frequency $f = 0.0567$. The associated dominate DMD mode is similar to those found by DFT and POD.

B. Global body forcing and optimal actuator placement

One question we are interested in is the optimal location of an actuator. As discussed in the previous section, the optimal forcing mode gives insight into this question, since it gives the forcing term (of unit norm) that has the largest amplification. We first present results of input-output analysis considering global body forcing distributed in the whole domain. Because the body force is global instead of local, the optimal forcing mode will shed light on the optimal actuator placement.

Assuming sinusoidal forcing in both time and the spanwise direction, the output will also be sinusoidal (in time and the spanwise direction), because the system is linear. Let

$$\boldsymbol{f}(x, y, z, t) = \hat{\boldsymbol{f}}(x, y)e^{i(k_z z + \omega t)}, \quad \boldsymbol{u}(x, y, z, t) = \hat{\boldsymbol{u}}(x, y)e^{i(k_z z + \omega t)}.$$

We consider only two-dimensional forcing in this study, i.e., $k_z = 0$. For each ω, we have a different transfer function, and

therefore different set of optimal forcing modes and response modes. We consider a particular frequency ω determined from the simulation previously described as "case B." From a power spectral density analysis of the streamwise velocity of a probe in the separation bubble, a (non-dimensional) peak frequency of $f_p = 0.06$ is found, which corresponds to the natural frequency of the separation bubble [19]. This frequency is also very close to the dominate frequency found from discrete Fourier transform of the full fluctuation velocity field. To report the result, we set $\omega_p = 2\pi f_p = 0.377$. The first eight singular values computed by randomized SVD are shown in Fig. 6 (a). The first singular value and singular vector change no more than 1% when we increase the number of random vectors in the randomized SVD algorithm by a factor of 2, verifying the convergence of the algorithm.

We observe that the first singular value is six orders of magnitude larger than the second and the rest, so the transfer function may indeed be approximated by an operator of rank one. To study the validity of rank-one approximation for other frequencies, we show the first three singular values of the transfer function (found by randomized SVD algorithm) for frequency ω varying around ω_p in Fig. 6 (b). It is verified that rank-one approximation is valid for a range of frequencies. Furthermore, we find that $\omega_p = 0.337$ has the maximum amplification among all the frequencies around it. This is consistent with the common practice to force the flow at its natural frequency.

The optimal response mode and optimal forcing mode are shown in Fig. 7. The energy in the optimal response mode is mainly concentrated in the streamwise and wall-normal component $(\hat{u}, \hat{v})$. The spanwise response $\hat{w}$ is found to be five orders of magnitude smaller than $\hat{u}, \hat{v}$. Only two-dimensional disturbances are considered here, so we do not expect a response in spanwise component. Recall that the optimal response mode is the dominant response to disturbances in the flow. The response is primarily in and behind the trailing edge of the separation bubble, from $x = 40\delta$ to $x = 70\delta$. Therefore, the separation bubble is receptive to disturbances.

As for the optimal forcing mode, we find that $\hat{f}_y$ is much smaller than $\hat{f}_x$, and $\hat{f}_z$ is nine orders of magnitude smaller than $\hat{f}_x$. Therefore, only the streamwise component $\hat{f}_x$ of the forcing is shown. The optimal forcing mode reveals that streamwise body force disturbance is much more important. However, ZNMF actuator produces disturbances mainly in the wall-normal direction. This result implies that a more effective actuator should instead introduce streamwise disturbances, which are much more efficient at exciting a response in the separation bubble. The optimal forcing energy is distributed along the wall, upstream of the separation bubble. Upstream disturbances to the flow travel downstream and produce a response in the separation bubble. This observation indicates that an actuator should be placed upstream, as in previous studies [1, 5]. The forcing mode also shows similarity with the optimal disturbances in the Blasius boundary layer reported in [27]. In [27], the optimal initial condition leading to the largest growth at finite times and the optimal time-periodic forcing leading to the largest asymptotic response are both considered.

The streamwise optimal forcing alternates between positive and negative values in the upstream region. Recall from Eq. 4 that the response is approximately proportional to the projection of the forcing in the direction of the optimal forcing mode ϕ_1. When the forcing is applied in both the positive region and negative region, their responses will be out of phase, and cancel each other. Typically, the location of a ZNMF actuator (which resembles a local body force) is not well tuned due to lack of physical insight. The optimal forcing mode suggests that the body force actuator should be carefully placed in order to avoid cancellation in the response.

C. Local body forcing

The governing equation Eq. (5) is spatially semi-discretized and put into state space form. Then we can derive the corresponding transfer function. We are mainly interested in local body forcing near the upstream of the wall. Consider local body forcing in the region $(x/\delta, y/\delta) \in \Omega$, where $\Omega = [0, 15] \times [0, 3]$. This can be achieved by choosing $b(\boldsymbol{x})$ to be 1 in Ω and 0 elsewhere in Eq. (5).

Similar to global forcing, randomized SVD algorithm is used to compute the leading singular values and singular vectors of the transfer function. The singular values for the case of $\omega_p = 0.337$ is presented in Fig. 8 (a). In addition, the first three singular values for a range of frequencies ω is shown in Fig. 8 (b). We conclude that rank-one approximation is valid for a range of frequencies ω. The optimal forcing and response mode corresponding to ω_p is illustrated in Fig. 9. Again the wall-normal forcing mode is much smaller and thus not shown here. Observe that both the response mode and forcing mode are almost identical to those found by global body forcing.

D. Implications and future work

In this part we will further discuss the implications of input-output analysis. While the preceding analysis provides insight about where and how to force the flow field, we still need to validate these implications numerically. We will outline the future work.

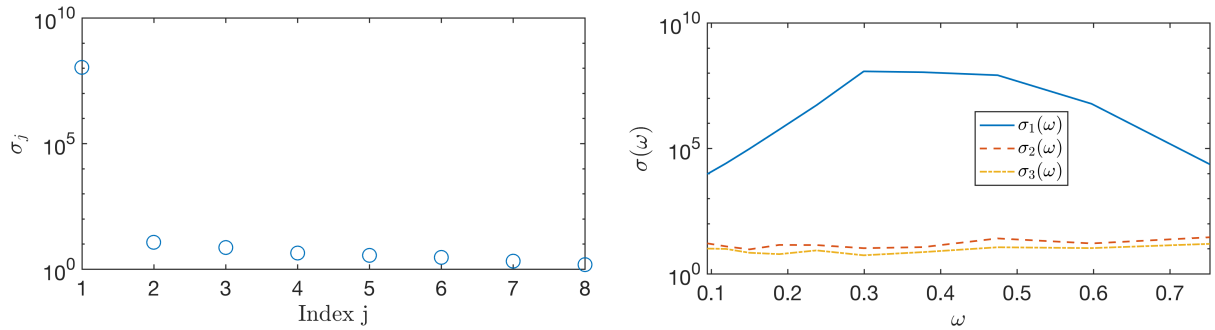

(a) **(b)**

Fig. 8 Local forcing result. (a) Singular values of the linear operator (transfer function) for $k_z = 0, \omega_p = 0.377$. (b) First three singular values of the transfer function for a range of frequency ω around ω_p. $k_z = 0$ is fixed.

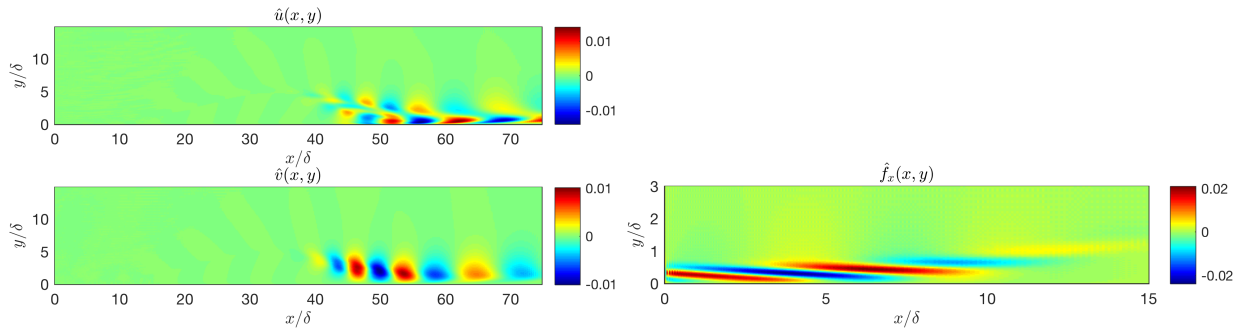

(a) **(b)**

Fig. 9 Local forcing result. (a) Streamwise and wall-normal optimal response mode $\hat{u}, \hat{v}$. $k_z = 0, \omega = 0.377$. (b) Streamwise optimal forcing mode $\hat{f}_x$.

Experiment	Simulation	Description
1	S1A	streamwise forcing placed upstream near the wall
	S1B	streamwise forcing placed upstream away from the wall
2	S2A=S1A	see S1A
	S2B	wall-normal forcing applied at the same region as streamwise forcing
3	S3A=S1A	see S1A
	S3B	streamwise forcing with the same shape but different orientation

Table 1 Setup of three control experiments. Each control experiment consists of two numerical simulations.

Based on the discussion in III.B, the optimal forcing mode is concentrated upstream near the wall, and streamwise forcing is much more important (compared with wall-normal forcing). In addition, the forcing mode consists of patches alternating between positive and negative values. As a result, in order to get large response, one should pay attention to this pattern to avoid cancellation effects.

In order to validate these implications, we will do three control experiments. There are two simulations in each. The first experiment aims to show that forcing should be applied upstream near the wall. The second experiment is designed to validate that streamwise forcing is more important than wall-normal forcing. The third experiment is intended to demonstrate the cancellation effect due to the pattern in the forcing mode . Details about these three experiments are summarized in Table. 1. To better describe the control experiments, we present visualization of the simulation setup in Fig. 10.

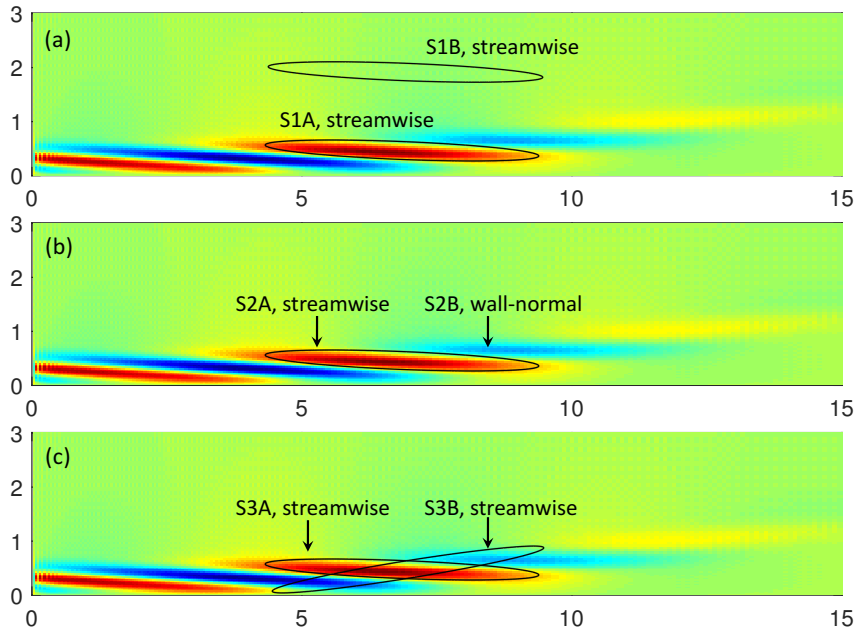

Fig. 10 (a) Experiment 1: forcing should be concentrated upstream near the wall. (b) Experiment 2: streamwise forcing is more important than wall-normal forcing. (c) Experiment 3: there exists cancellation effect

IV. Conclusion

In this study we performed input-output analysis for a separated flow past a flat plate. The body forcing (global or local) is taken as input, and flow field is taken as output. A transfer function that maps input to output can be derived by assuming sinusoidal forcing in time. It is validated that the transfer function is indeed approximately rank-one. The forcing mode corresponds to the maximum amplification in the response provides insight about optimal forcing location and frequency.

We find that the when the flow is forced at the natural frequency of the separation bubble, the response is maximized (in terms of energy). The response is mainly in and behind the trailing edge of the separation bubble, demonstrating the receptivity of the separation bubble to body forcing. Furthermore, the forcing mode indicates the optimal forcing location is upstream near the wall. In order to get a large response, one should carefully place the forcing in the upstream region, to avoid cancellation effects.

In future work, we will perform numerical simulation to validate these implications. In particular, we would like to verify that (a) the optimal forcing should be concentrated upstream near the wall, (b) streamwise is the optimal forcing direction, and (c) there exists a cancellation effect in the response.

Acknowledgments

This material is based upon work supported by the Air Force Office of Scientific Research under award number FA9550-17-1-0084.

References

[1] Mittal, R., Kotapati, R., and Cattafesta, L., "Numerical study of resonant interactions and flow control in a canonical separated flow," *43rd AIAA Aerospace Sciences Meeting and Exhibit*, 2005, p. 1261.

[2] Seifert, A., Darabi, A., and Wyganski, I., "Delay of airfoil stall by periodic excitation," *Journal of Aircraft*, Vol. 33, No. 4, 1996, pp. 691–698.

[3] Glezer, A., Amitay, M., and Honohan, A. M., "Aspects of low-and high-frequency actuation for aerodynamic flow control," *AIAA Journal*, Vol. 43, No. 7, 2005, pp. 1501–1511.

[4] Mittal, R., and Kotapati, R. B., "Resonant mode interaction in a canonical separated flow," *IUTAM Symposium on Laminar-Turbulent Transition*, Springer, 2006, pp. 341–348.

[5] Raju, R., Mittal, R., and Cattafesta, L., "Dynamics of airfoil separation control using zero-net mass-flux forcing," *AIAA Journal*, Vol. 46, No. 12, 2008, pp. 3103–3115.

[6] Glezer, A., and Amitay, M., "Synthetic jets," *Annual Review of Fluid Mechanics*, Vol. 34, No. 1, 2002, pp. 503–529.

[7] Seifert, A., Greenblatt, D., and Wygnanski, I. J., "Active separation control: an overview of Reynolds and Mach numbers effects," *Aerospace Science and Technology*, Vol. 8, No. 7, 2004, pp. 569–582.

[8] Melton, L. P., Yao, C. S., and Seifert, A., "Active control of separation from the flap of a supercritical airfoil," *AIAA Journal*, Vol. 44, No. 1, 2006, pp. 34–41.

[9] Deem, E. A., Cattafesta, L. N., Yao, H., Hemati, M., Zhang, H., and Rowley, C. W., "Experimental implementation of modal approaches for autonomous reattachment of separated flows," *2018 AIAA Aerospace Sciences Meeting*, 2018, p. 1052.

[10] Jovanović, M. R., and Bamieh, B., "Componentwise energy amplification in channel flows," *Journal of Fluid Mechanics*, Vol. 534, 2005, pp. 145–183.

[11] McKeon, B., and Sharma, A., "A critical-layer framework for turbulent pipe flow," *Journal of Fluid Mechanics*, Vol. 658, 2010, pp. 336–382.

[12] Luhar, M., Sharma, A. S., and McKeon, B. J., "Opposition control within the resolvent analysis framework," *Journal of Fluid Mechanics*, Vol. 749, 2014, pp. 597–626.

[13] Garnaud, X., Lesshafft, L., Schmid, P., and Huerre, P., "The preferred mode of incompressible jets: linear frequency response analysis," *Journal of Fluid Mechanics*, Vol. 716, 2013, pp. 189–202.

[14] Jeun, J., Nichols, J. W., and Jovanović, M. R., "Input-output analysis of high-speed axisymmetric isothermal jet noise," *Physics of Fluids*, Vol. 28, No. 4, 2016, p. 047101.

[15] Gómez, F., Blackburn, H., Rudman, M., Sharma, A., and McKeon, B., "A reduced-order model of three-dimensional unsteady flow in a cavity based on the resolvent operator," *Journal of Fluid Mechanics*, Vol. 798, 2016.

[16] Taira, K., Brunton, S. L., Dawson, S., Rowley, C. W., Colonius, T., McKeon, B. J., Schmidt, O. T., Gordeyev, S., Theofilis, V., and Ukeiley, L. S., "Modal analysis of fluid flows: An overview," *arXiv preprint arXiv:1702.01453*, 2017.

[17] Yeh, C.-A., and Taira, K., "Resolvent-analysis-based design of airfoil separation control," *arXiv preprint arXiv:1805.02128*, 2018.

[18] Mohammed-Taifour, A., and Weiss, J., "Unsteadiness in a large turbulent separation bubble," *Journal of Fluid Mechanics*, Vol. 799, 2016, pp. 383–412.

[19] Wu, W., Seo, J.-H., Meneveau, C., and Mittal, R., "Response of a laminar separation bubble to forcing with zero-net mass flux jets," *AIAA Journal to appear*, 2018.

[20] Mittal, R., Dong, H., Bozkurttas, M., Najjar, F., Vargas, A., and von Loebbecke, A., "A versatile sharp interface immersed boundary method for incompressible flows with complex boundaries," *Journal of Computational Physics*, Vol. 227, No. 10, 2008, pp. 4825–4852.

[21] Seo, J., Cadieux, F., Mittal, R., Deem, E., and Cattafesta, L., "Effect of synthetic jet modulation schemes on the reduction of a laminar separation bubble," *Physical Review Fluids*, Vol. 3, No. 3, 2018, p. 033901.

[22] Beneddine, S., Sipp, D., Arnault, A., Dandois, J., and Lesshafft, L., "Conditions for validity of mean flow stability analysis," *Journal of Fluid Mechanics*, Vol. 798, 2016, pp. 485–504.

[23] Halko, N., Martinsson, P.-G., and Tropp, J. A., "Finding structure with randomness: Probabilistic algorithms for constructing approximate matrix decompositions," *SIAM Review*, Vol. 53, No. 2, 2011, pp. 217–288.

[24] Lumley, J. L., "The structure of inhomogeneous turbulent flows," *Atmospheric Turbulence and Radio Wave Propagation*, 1967.

[25] Schmid, P. J., "Dynamic mode decomposition of numerical and experimental data," *Journal of Fluid Mechanics*, Vol. 656, 2010, pp. 5–28.

[26] Rowley, C. W., and Dawson, S. T., "Model reduction for flow analysis and control," *Annual Review of Fluid Mechanics*, Vol. 49, 2017, pp. 387–417.

[27] Monokrousos, A., Åkervik, E., Brandt, L., and Henningson, D. S., "Global three-dimensional optimal disturbances in the Blasius boundary-layer flow using time-steppers," *Journal of Fluid Mechanics*, Vol. 650, 2010, pp. 181–214.